

# Complementary interactions of orbital momentum and topological spin states in ferromagnet/Cu/Bi<sub>0.85</sub>Sb<sub>0.15</sub> structures

Shu Hui Lee<sup>1,2</sup>, Calvin Ching Ian Ang<sup>1</sup>, Han Yin Poh,<sup>2</sup> Gerard Joseph Lim,<sup>1</sup> Tianli Jin,<sup>1</sup> Wanbing Yi,<sup>2</sup> and Wen Siang Lew<sup>1,\*</sup>

<sup>1</sup>*School of Physical and Mathematical Sciences, Nanyang Technological University, 21 Nanyang Link, Singapore 637371, Singapore*

<sup>2</sup>*Technology Development, GlobalFoundries Singapore Pte. Ltd., 60 Woodlands Industrial Park D Street 2, Singapore 738406, Singapore*



(Received 22 July 2024; revised 17 January 2025; accepted 28 March 2025; published 2 May 2025)

Topological insulator spin-momentum locked surface states have been of interest for their contribution to highly efficient charge-to-spin conversion. However, the potential interactions between spin states in topological insulators and orbital momentum from light metals remain unexplored. Here, leveraging orbital and spin torques in the ferromagnet/Cu/Bi<sub>0.85</sub>Sb<sub>0.15</sub> heterostructure, a significant enhancement in dampinglike spin efficiency of up to six times is observed. We establish that the underlying mechanism for the improvement is due to the enhanced crystallinity of the topological insulator when Cu is used as an interlayer, coupled with substantial bulk orbital momentum generated by the light metal Cu. This complementary combination of topological insulators and light metals exceeds their individual contributions, laying critical groundwork for effective performance.

DOI: 10.1103/PhysRevApplied.23.054003

## I. INTRODUCTION

Investigating the fundamental mechanisms responsible for the spin Hall effect has contributed to the discovery of topological physics [1–21], as well as of the orbital Hall and orbital Rashba effects [22–36]. In a 3D topological insulator (TI), topologically protected spin-polarized surface states surround topologically insulating bulk states with a preserved time-reversal symmetry [8–21]. These topological spin-polarized textures can be electrically conducted into the ferromagnet to produce nonequilibrium spin torques on magnetization [37,38]. The TI-induced spin torques produce a large dampinglike field, which enables the ultralow-powered electrical control of magnetization. One key property of TIs is the resistance of topological surface states to lattice distortions or defects due to time-reversal symmetry [3,21]. This property has enabled TIs, such as BiSb, to be sputtered and display large spin torques in charge transport measurements [8–11,37–50]. In BiSb, the crystallographic orientation of the BiSb(012) plane intersects the Brillouin zone across three Dirac cones at  $\bar{\Gamma}$ ,  $\bar{M}$ , and  $\bar{X}$ , which is most crucial for spin-torque generation [40].

Apart from TIs, heavy metals (HMs) have been the conventional spin-torque source, which utilizes strong

spin-orbit coupling to generate and inject spin currents into adjacent ferromagnets (FMs). However, in sharp contrast, light metals with weak spin-orbit coupling have been rigorously studied in recent years as a new family of torque sources [25–36]. In light metals, orbital torque arises from the transverse momentum generated in localized electron orbitals under an externally applied electric field that can exert torque on magnetic films even under weak spin-orbit coupling (SOC) [31–35]. Leveraging the complementary effects of the light metals and the 3D topological insulators holds significant promise for enhancing spin-torque efficiency.

Here, we investigated the dampinglike spin-torque efficiency for a range of thin interlayer materials, including Cu, Ti, and Pt, in a perpendicularly magnetized [Pt/Co]<sub>6</sub> multilayer and polycrystalline BiSb heterostructure. The Cu interlayer demonstrated the strongest enhancement in dampinglike efficiency, owing partly to the improved BiSb(012) crystallinity when deposited on top of the Cu layer, as verified via an x-ray diffraction (XRD) analysis (for details, see Figs. 5–8 within the Appendix). When the thickness of the Cu interlayer is increased, the partial contribution of the orbital torques from the bulk of the Cu layer property was observed. Several permutations of the FM/Cu/BiSb heterostructure were fabricated to conclusively demonstrate the complementary natures of the Cu and BiSb layers that generate torque beyond their individual contributions.

\*Contact author: wensiang@ntu.edu.sg

## II. EXPERIMENTAL PROCEDURE

Figure 1(a) shows a schematic of the sample structures. All the samples were grown at room temperature by using an AJA ultrahigh vacuum magnetron sputtering system. The base pressure was below  $6 \times 10^{-8}$  Torr and the sputtering pressure was 2 mTorr with an argon flow rate of 20 sccm.

Co, Pt, and Ti were deposited using 50 W of dc power, while BiSb was deposited using 25 W of rf power. Deposition rates were calibrated using atomic force microscopy (AFM) measurements of the film thickness over extended deposition periods (700–1000 s) per material.

A Ti (2 nm) seed layer was deposited on Si/SiO<sub>2</sub> substrates for good film adhesion. The deposited ferromagnetic [Pt/Co]<sub>6</sub> multilayer, which has perpendicular magnetization, was first sputter-grown on silicon substrates, followed by an interlayer/BiSb stack. Different interlayer materials consisting of Cu, Ti, and Pt were chosen for investigation. The bottom and top Ti (2 nm) layers served as adhesion and capping layers, respectively. Spin-torque efficiency was obtained by measuring  $V_\omega$  and  $V_{2\omega}$  with respect to a longitudinal magnetic field regime [51]. The adiabatic frequency of the alternating charge current was 307.1 Hz. The charge current density  $j_{AC}$  was varied in steps of  $1 \times 10^9$  Am<sup>-2</sup> from  $2.5 \times 10^{10}$  to  $3.0 \times 10^{10}$  Am<sup>-2</sup>, corresponding to an applied alternating charge current of 0.20–0.24 A prior to insertion of any interlayer. The applied charge current changed accordingly with the addition of a thicker interlayer, maintaining the same applied charge current densities per measurement. The cross-sectional width and height were 30  $\mu$ m and  $(40.4 + x)$  nm, where  $x$  refers to the thickness of the interlayer.

## III. RESULTS AND DISCUSSION

Cu and Ti are light spin-orbit coupling materials as opposed to the heavy metal Pt, which has strong SOC. These interlayers are grown below the BiSb layer, leading to a significant influence on the BiSb crystal growth. Figure 1(b) shows the resulting dampinglike field per unit charge current density  $H_{DL}/j_{BiSb}$  measured by using the harmonic Hall technique [51]. The baseline  $H_{DL}/j_{BiSb}$  from that of the BiSb layer without any interlayer was high at  $(640 \pm 20)$  Oe MA<sup>-1</sup> cm<sup>2</sup> due to the large spin Hall conductivity of BiSb [40]. The measurements show that the insertion of the heavy Pt and light Ti interlayers in the heterostructures does not have any major impact on the enhancement of the spin torque. In contrast, the insertion of light metal Cu interlayer has contributed to the rapid increase of efficiency, up to 136% at 2 nm. In the following sections, the mechanisms of the enhancement are discussed and experimentally assessed.

The XRD measurements of the heterostructures reveal that only the Cu interlayer heterostructure enables a clear improvement to the BiSb(012) diffraction peak intensity, while that of the other interlayer materials have weakened, as shown in Fig. 2(a). The extractions of the full-width half maximum (FWHM) from the diffraction peaks via Gaussian fitting (the details can be found in Fig. 5 within the Appendix) and the estimation of the crystallite size,  $D$ , through the Scherrer equation,  $D = K\lambda/\text{FWHM}(2\theta) \cos(\theta)$  [52], as shown in Fig. 2(b), confirm an aligned result where only the Cu interlayer heterostructure shows improved crystallinity. The complementary alignment in trend between spin-torque efficiency from Fig. 1(b) and crystallite size in Fig. 2(b) implies the correlation of BiSb(012) ordering to the measured spin-torque efficiency in the FM/spacer/BiSb

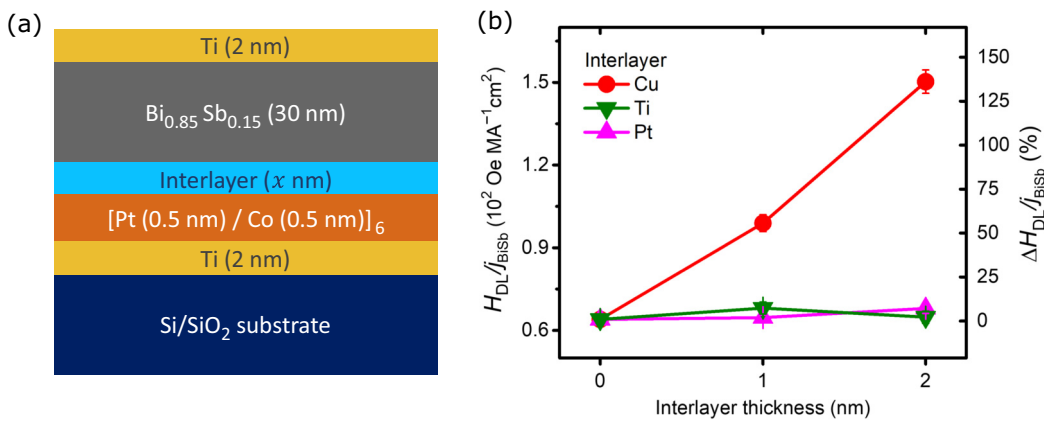


FIG. 1. (a) Schematic of the stack structures, where different interlayer materials of Cu, Ti, or Pt are chosen for investigation. (b) Measurements of the dampinglike efficiency, normalized to charge current density in the BiSb, for different interlayer thicknesses and materials.

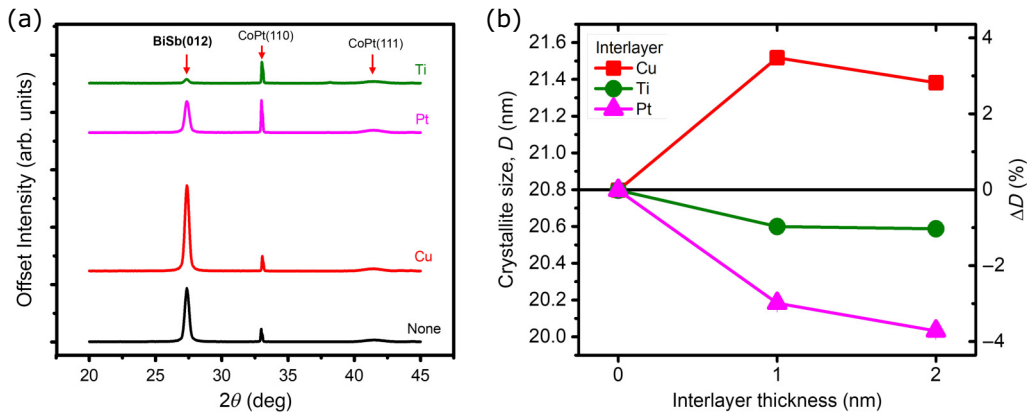


FIG. 2. (a) XRD plots of the measured BiSb(012) peaks for each sample with a Pt, Ti, and Cu interlayer, and (b) the BiSb(012) crystallite sizes of the samples extracted from the XRD measurements as the interlayer thicknesses are varied.

structures. The increased crystallinity of the BiSb(012) planes, observed from the increasing crystallite size, supports spin-torque generation [40,50] from the topological insulator layer.

To probe the origins of these observed complementary effects, the Cu interlayer thickness-dependent damping-like spin-torque efficiency per unit charge current density ( $\xi_{\text{DL}}^j$ ) measurements were carried out; the results are shown in Fig. 3(a). By varying the Cu interlayer thickness up to 10 nm, the dampinglike spin-torque efficiency per unit charge current density,

$$\xi_{\text{DL}}^j = \frac{2e}{\hbar} t_{\text{FM}} M_S \frac{H_{\text{DL}}}{j_{\text{BiSb}}},$$

increases and peaks at an interlayer Cu thickness of 7 nm with  $\xi_{\text{DL}}^j = 65 \pm 3$  before decreasing with larger Cu thicknesses.

In probing the linkage between crystallinity and the spin-current behavior, the measurement of the XRD peaks across  $2\theta$  reveals strong BiSb(012) intensity and resolution with an increasing crystallite size up to 5 nm. This suggests that the Cu interlayer promotes the increase of spin torques due to Dirac state formation [40] from crystallinity-related mechanisms up to 5 nm. Figure 3(b) shows that the BiSb crystallite size increases with larger Cu thickness and the BiSb(012) crystallinity reaches an optimum level with a plateau at 3–5 nm. Beyond 5 nm, it degrades at  $\sim 1.0\text{--}1.5\%$  per nanometer with a further increase of the Cu thickness. This implies that the BiSb(012) crystallinity accounts for  $\xi_{\text{DL}}^j$  with thinner interlayers between 0 to 5 nm, beyond which the continued increase in  $\xi_{\text{DL}}^j$  suggests the presence of a bulk effect scaling with the Cu interlayer thickness.

Both the trend of increasing spin-torque efficiency,  $\xi_{\text{DL}}^j$ , and crystallite sizes,  $D$ , align at small Cu thicknesses. However, for Cu thicknesses above 5 nm, the  $\xi_{\text{DL}}^j$  value continually rises to its peak at about 8 nm while the

BiSb(012) crystallite size starts to degrade. While part of the increase in the  $\xi_{\text{DL}}^j$  values can be attributed to the improved BiSb crystallinity, the divergent trend of the  $\xi_{\text{DL}}^j$  values and the BiSb(012) crystallite size within a Cu thickness of 3–7 nm suggests that the Cu interlayer partly accounts for the peaking of the  $\xi_{\text{DL}}^j$  value at 8 nm, independent from the BiSb(012) crystallinity factor above a Cu thickness of 5 nm. Thus, both the conduction of the spin-current and the orbital torques generated in the Cu interlayer contribute to the total torque exerted on the FM. Moreover,  $\xi_{\text{DL}}^j$  is limited at larger Cu thicknesses beyond its peak value due to the detriment of the worsening BiSb crystallinity overcoming the improvements introduced by Cu.

Figure 3 shows that spin-torque efficiency remains elevated due to the bulk orbital Hall contributions, even beyond crystallinity peaks at intermediate Cu thicknesses, highlighting the complementary roles of BiSb(012) crystallinity and orbital momentum generation and transfer for enhancing spin-torque performance. This interplay is a central theme of our study; we have carefully designed our experimental framework to capture and analyze these mechanisms.

At ultrathin Cu interlayer thicknesses, spin-torque efficiency strongly correlates with BiSb(012) crystallinity, indicating a dominant interfacial contribution. In contrast, at larger Cu thicknesses, the systematic enhancement of the orbital momentum is reflected by the increased spin-torque efficiency, demonstrating significant bulk contributions from the Cu interlayer.

The observed deviations between the BiSb(012) crystallite size and spin-torque efficiency underscore the complementary roles of these mechanisms. Specifically, while crystallinity peaks at intermediate Cu thicknesses, torque efficiency remains elevated due to the bulk orbital Hall contributions, which operate independently and collaboratively with interfacial topological surface states.

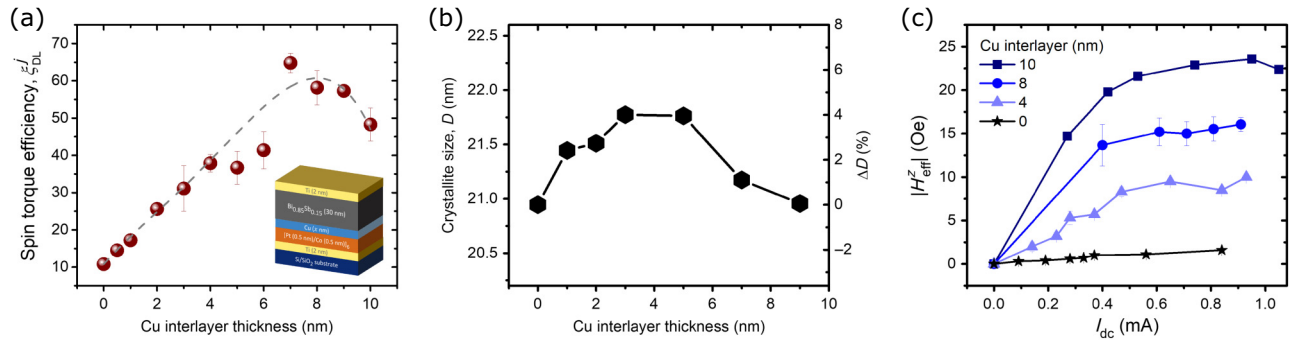


FIG. 3. (a) Measurements of the spin-orbit torque efficiency across a range of Cu interlayer thicknesses. The dotted lines serve as a guide for the eyes. (b) Change in crystallite size of BiSb(012) with Cu interlayer thickness. (c) Average induced out-of-plane effective field  $H_{eff}^z$  for the Cu interlayer samples over the absolute value of direct current  $I_{dc}$  injected under an in-plane field  $H_x = +2$  kOe and an externally applied out-of-plane field  $H_z = +220$  Oe.

To characterize the switching behavior of the samples, the induced effective out-of-plane field  $H_{eff}^z$  was measured and plotted over the applied absolute direct current. Here,  $H_{eff}^z$  reflects the effective out-of-plane field exerted by switching torques, which has been widely used in various studies to characterize trends in spin-torque efficiency [53–55]. The parameter  $H_{eff}^z$  provides a robust indication of the efficiency of switching torques, particularly in systems where direct switching measurements are hindered by high coercivity, which ensures measurements are not confounded by stochastic effects prevalent in low coercivity systems.

As shown in Fig. 3(c),  $H_{eff}^z$  increases systematically with greater Cu interlayer thickness. At an absolute direct current of 0.8 mA, a maximum  $H_{eff}^z$  is 14.6 and 4.83 times higher in 10-nm Cu and 4-nm Cu samples, respectively, compared with a 0-nm Cu sample. This enhancement is attributed to the enlarged orbital momentum generated by the additional Cu atomic layers, which amplifies the spin Hall angle by providing a stronger source for spin-torque conversion in the ferromagnetic layer. The observed improvement in  $H_{eff}^z$  directly reflects spin-torque efficiency driven by the orbital Hall and orbital momentum transfer effects.

To uncover the interplay between the Cu interlayer and the BiSb layer that provides the observed large spin torque, a series of samples with permutations of the FM/Cu/BiSb heterostructure and reference samples were fabricated, and their  $\xi_{DL}^j$  values were measured, as shown in Fig. 4(a). Firstly, by comparing FM/Ti (2 nm), FM/Cu(2 nm), and FM/Pt(2 nm), i.e., Samples S1, S2, and S3, respectively, we note that for the same interlayer thickness, Sample S3 has a larger  $\xi_{DL}^j$  value of  $0.51 \pm 0.01$  due to the property of a large spin-orbit coupling in the heavy metal Pt. However, when the Cu thickness was increased from 2 to 10 nm in Sample S4, the  $\xi_{DL}^j$  value increased further to  $1.6 \pm 0.2$ ,

consistent with the presence of strong orbital torque originating from the light metal. On the other hand, Sample S7, i.e., FM/BiSb, has a significantly larger  $\xi_{DL}^j$  value at  $10.8 \pm 0.7$  for the contributions from the TI property. By using the Cu(10 nm) as an interlayer between the FM and the BiSb film, as revealed by the measurement of Sample S5, the  $\xi_{DL}^j$  value increases significantly to  $50 \pm 12$ , exceeding the individual contributions by Cu and BiSb. This result suggests that the pairing of Cu as an interlayer with BiSb leads to greater spin-torque efficiency per unit current density than from the individual Cu or BiSb thin films alone due to a combination of BiSb(012) crystallinity and orbital torques arising from the Cu interlayer.

To further clarify any interfacial effects at the Cu/BiSb interface, an additional sample with a 1-nm-thick MgO layer inserted between the Cu and the BiSb was prepared. The measured dampinglike spin efficiency per unit current density value,  $\xi_{DL}^j$ , of the sample with the disrupted Cu/BiSb interface was lowered by 22% to  $37.3 \pm 0.7$  but remains significantly larger than that of the BiSb without any interlayer, i.e.,  $10.8 \pm 0.7$ . Thus, the interfacial contribution of the Cu/BiSb interface plays a minimal role in the spin torque, while the bulk of the Cu layer contributes significantly to the  $\xi_{DL}^j$  enhancement originating from orbital torques.

The observed 25% reduction of the spin Hall angle upon MgO insertion in Fig. 4(a) can be attributed to a combination of factors, including crystallinity degradation and spin transmission limitations. The minor decrease in BiSb crystallinity likely reduces the quality of topological surface states, partially accounting for the reduced spin-torque efficiency. Additionally, the MgO layer, acting as an insulator, introduces additional resistance to spin-current transmission across the interface, providing a further contribution to the observed reduction. These factors, considered together, suggest that the contribution of

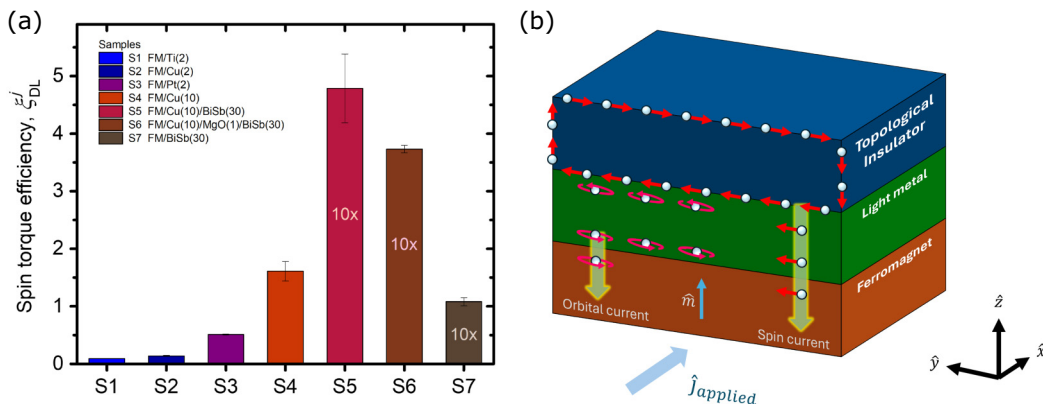


FIG. 4. (a) Comparison of the dampinglike spin-torque efficiency,  $\xi_{DL}^j$ , with respect to a variety of materials and their thicknesses, i.e., Ti, Cu, Pt, and BiSb. The actual  $\xi_{DL}^j$  values of Samples S5–S7 are scaled down by ten times, indicated by the words in white, for ease of visual comparison with the significantly smaller  $\xi_{DL}^j$  values for Samples S1–S3. (b) Schematic of the complementary effects from spin and orbital torques acting upon the ferromagnet under an applied current density,  $j_{applied}$ .

the Cu/BiSb interface to the total spin-torque efficiency is minimal.

Furthermore, our data indicates that the Cu/BiSb interface does not dominate the spin Hall angle enhancement. This conclusion is further supported by the linear trend in spin-torque efficiency observed as a function of Cu thickness in Fig. 3(a). If interfacial Rashba effects were significant, we would expect a sharp increase in spin efficiency at the lowest Cu thicknesses, followed by a decrease toward saturation. Instead, the monotonic increase at the narrower Cu thicknesses suggests that bulk and crystallinity effects are the primary contributors to the observed efficiency.

In summary, the observed 25% reduction in the spin Hall angle after MgO insertion can be largely explained by crystallinity degradation and spin transmission limitations due to the insulating nature of MgO, as supported by additional XRD measurements (for the details, see the comparison of BiSb(012) crystallinity in the Cu/BiSb and Cu/MgO/BiSb samples in Fig. 9 within the [Appendix](#)). This supports the explanation that the Cu/BiSb interfacial effects have negligible contributions to the spin Hall angle enhancement. Our findings are consistent with a predominantly bulk-driven mechanism for the observed complementary effects.

As explained earlier, the results analyzed suggest the presence of a complementary effect from spin and orbital torques with BiSb(012) crystallinity in the Cu/BiSb heterostructure. The mechanism is illustrated in Fig. 4(b), where improved BiSb(012) crystallinity increases the spin-current injection into the FM. The spin-momentum-locked Dirac states on the surface of the topological insulator are conducted into the FM through the light metal interlayer. By increasing the crystallinity of BiSb(012), the spin polarization of the momentum-locked states is reinforced and, thus, increases the spin torques registered in the FM.

Concurrently, another mechanism arises from the orbital Hall momentum formed within the bulk of the light metal layer under the applied electric field. The applied current density,  $j_{applied}$ , flowing through the Cu layer establishes a strong orbital Hall momentum in the bulk of the Cu layer, which scales with the Cu thickness. The observed decrease in spin-torque efficiency per unit current density from around 7 nm in Fig. 3(a) correlates with a drop in spin-polarized topological surface states, inferred from the slightly deteriorating crystallinity of the BiSb(012) plane from 7 nm in Fig. 3(b). The orbital Hall momentum transmits from the light metal layer bulk into the FM, where orbital torques are thus exerted. Taking both possible mechanisms into consideration, our results reveal a highly effective complementary spin torque achieved by pairing a light metal Cu with the topological insulator BiSb, which significantly enhanced the spin-torque efficiencies above that of constituent Cu or BiSb alone.

#### IV. CONCLUSION

In conclusion, the light metal Cu as an interlayer demonstrated a strong complementary enhancement of spin-torque efficiency for the perpendicular magnetization of a [Pt/Co] multilayer. The complementary enhancement utilized both the orbital torque from the bulk of the Cu layer and the improved BiSb(012) crystallinity of up to 4% using a Cu seed layer. Signatures of the orbital torque from the bulk of the Cu layer were observed via the six times enhancement of the spin Hall angle within the Cu/BiSb stack, as total torque increased steadily up to a larger Cu thickness of 7 nm. The complementary effects from the orbital and spin torques in the Cu/BiSb heterostructure observed in this work pave the way for an approach that surpasses incumbent TI spin-torque performance.

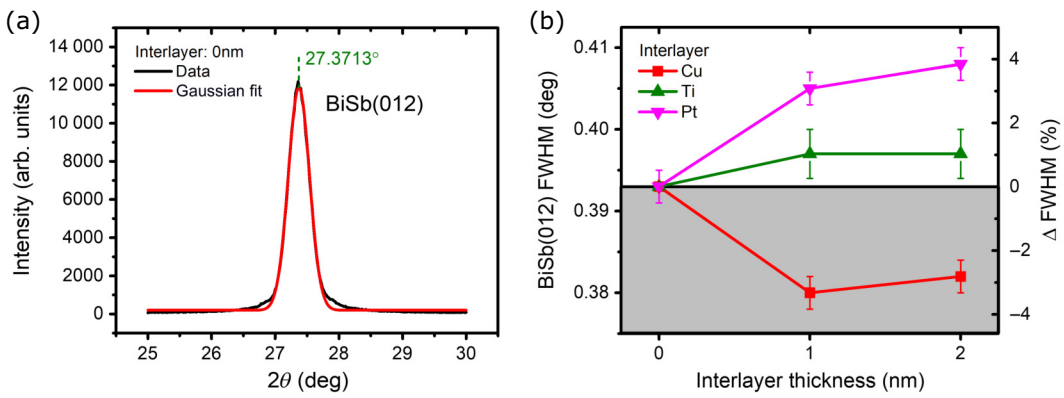


FIG. 5. (a) Gaussian fit of the BiSb(012) peak on the 0-nm interlayer XRD data. (b) BiSb(012) peak full-width half maximum (FWHM) taken from the Gaussian fit of the peaks for each different interlayer sample. The Cu interlayer sample peaks had the lowest FWHM.

## ACKNOWLEDGMENTS

This work was supported by the Ministry of Education (MOE) Singapore under the MOE Tier 1 grant (Grant No. RG76/23). The support from a RIE 2020 ASTAR AME IAF-ICP (Grant No. I1801E0030) and the Singapore Economic Development Board (EDB) under Grant No. 2021-REQ0265132 EDB-IPP are also acknowledged.

## DATA AVAILABILITY

The data that support the findings of this article are not publicly available. The data are available from the authors upon reasonable request.

## APPENDIX: XRD CALCULATIONS, $\text{Bi}_{0.85}\text{Sb}_{0.15}$ LATTICE CONSTANTS AND ANALYSIS, COMPARISON WITH THEORETICAL ESTIMATES OF BISB LATTICE CONSTANTS, AND XRD DATA FOR Cu/MgO/ $\text{Bi}_{0.85}\text{Sb}_{0.15}$

Figure 5(a) gives an example of how a Gaussian fit was used to extract the peak position of  $27.37^\circ$ , as well as the peak width or full-width half maximum (FWHM), in the Cu(0 nm) sample. This simple method was repeated for each of the peaks and across all the Cu interlayer samples. All peaks in the XRD plots were identified with the MATCH! XRD analysis software. We found in Fig. 5(b) that the Cu interlayer samples produced  $\text{Bi}_{0.85}\text{Sb}_{0.15}(012)$

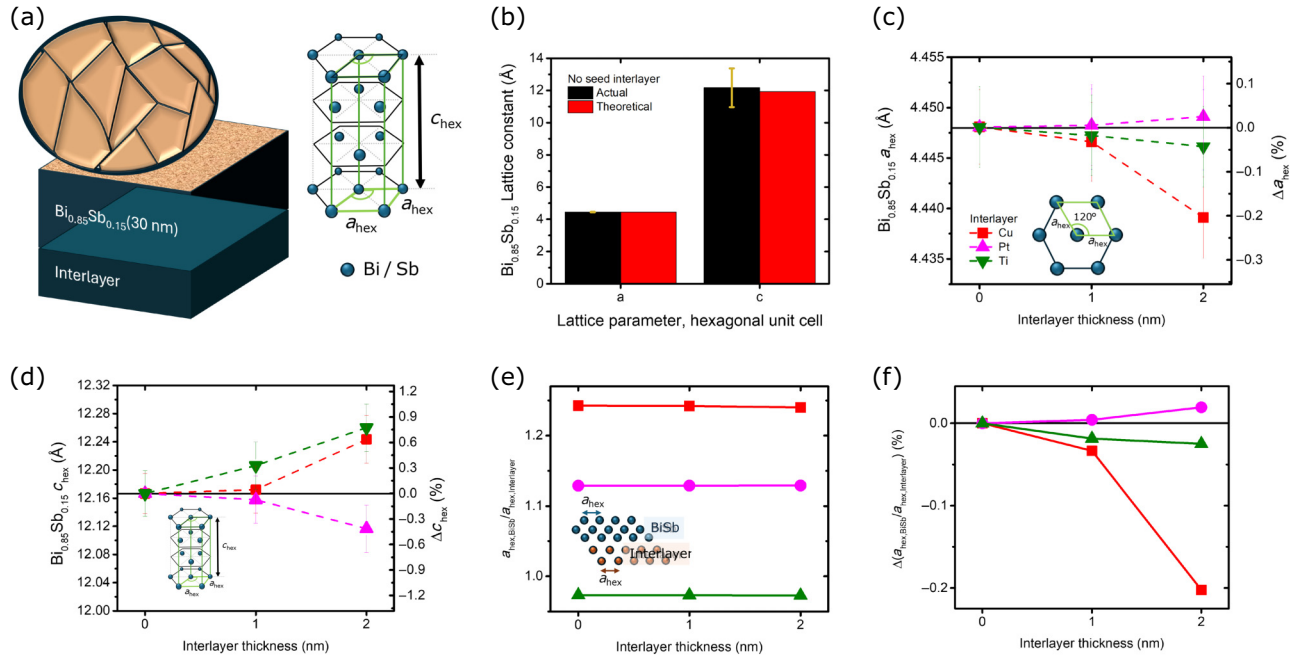


FIG. 6. (a) A schematic of the nanoscale crystalline domains and the atomic crystal lattice unit cell in BiSb grown atop the interlayer. (b) Lattice constants  $a_{\text{hex}}$  and  $c_{\text{hex}}$  of BiSb compared with their theoretical values. Cross-material comparisons for (c)  $a_{\text{hex}}$  and (d)  $c_{\text{hex}}$ . (e) Ratio of the intralattice spacing in BiSb and the interlayer,  $a_{\text{hex},\text{BiSb}}/a_{\text{hex},\text{Interlayer}}$ . (f) Percentage change in  $a_{\text{hex},\text{BiSb}}/a_{\text{hex},\text{Interlayer}}$  relative to the case in which no interlayer is present.

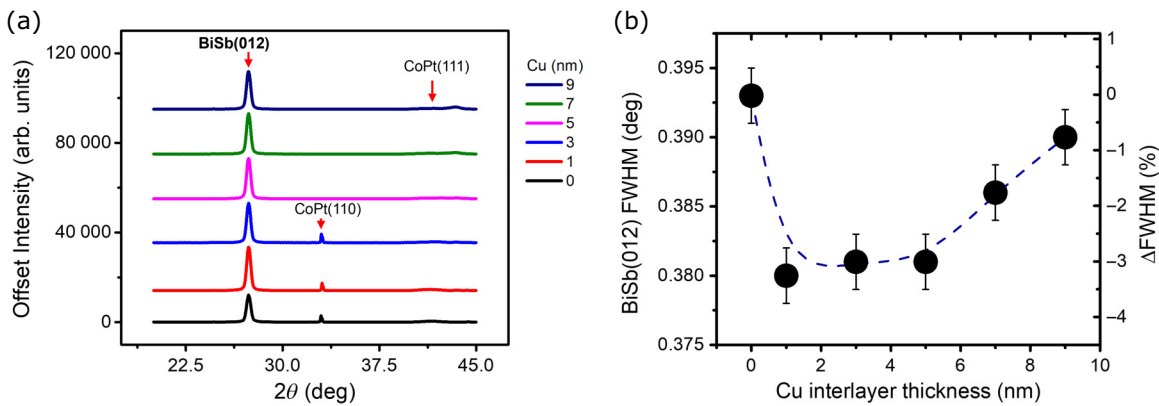


FIG. 7. (a) XRD plots cropped from  $22.5$  to  $45^\circ$ , highlighting the BiSb(012) lattice peaks, and (b) the full-width half maximum (FWHM) for Cu with  $1$ – $9$  nm interlayer thicknesses.

peaks of the lowest FWHMs, which indicated peaks that were the most defined with optimal lattice ordering in the  $\text{Bi}_{0.85}\text{Sb}_{0.15}$  films grown atop of the Cu interlayer samples.

Within each of the polycrystalline domains in sputtered  $\text{Bi}_{0.85}\text{Sb}_{0.15}$  on the Angstrom scale. The Bi and Sb atoms are ordered neatly [47] with 85% and 15% probability, respectively, into individual atomic positions in hexagonal unit lattices without dislocation [Fig. 6(a)]. Prior to interlayer insertion, the lattice constants  $a_{\text{hex}} = 4.448 \pm 0.001 \text{ \AA}$  and  $c_{\text{hex}} = 12.17 \pm 0.02 \text{ \AA}$  for  $\text{Bi}_{0.85}\text{Sb}_{0.15}$  match their theoretical values of  $4.45 \text{ \AA}$  and  $11.93 \text{ \AA}$  by 99.96% and 98.02%, respectively [Fig. 6(b)]. The theoretical values were provided by the Materials Project [56], a non-profit international effort to simulate and compute the material properties of inorganic materials.

The lattice constants that define the hexagonal unit cell of the  $\text{Bi}_{0.85}\text{Sb}_{0.15}$  lattice, i.e.,  $a_{\text{hex}}$  and  $c_{\text{hex}}$ , depend on

the interlayer material and thickness. After the addition of interlayers beneath  $\text{Bi}_{0.85}\text{Sb}_{0.15}$ , the lattice parameters are altered [Figs. 6(c) and 6(d)], causing varying degrees of  $a_{\text{hex}}$  lattice mismatch between  $\text{Bi}_{0.85}\text{Sb}_{0.15}$  and the interlayer [Fig. 6(e)]. Pt, Ti, and Cu demonstrate increasingly observable  $\Delta a_{\text{hex}}$  and  $\Delta c_{\text{hex}}$ . With an increasing Pt interlayer thickness beneath it, the  $\text{Bi}_{0.85}\text{Sb}_{0.15}$  lattice is slightly stretched along  $a_{\text{hex}}$ , which increases by up to 0.02% and is most significantly compressed as  $c_{\text{hex}}$  reduces by 0.41%. Ti causes  $a_{\text{hex}}$  to reduce by up to 0.04% and  $c_{\text{hex}}$  to increase by up to 0.77%, while Cu most greatly reduces  $a_{\text{hex}}$  by 0.2% and increases  $c_{\text{hex}}$  by 0.63%. For  $\text{Bi}_{0.85}\text{Sb}_{0.15}$  grown atop Ti and Cu, the lattice shrinks along  $a_{\text{hex}}$  and is pulled along  $c_{\text{hex}}$ . The largest decrease in  $a_{\text{hex}}$  using Cu, which is above 0.1% greater in magnitude compared with the change from any other interlayer, correlates strongly with the largest decrease in the  $\text{Bi}_{0.85}\text{Sb}_{0.15}$  intralattice spacing.

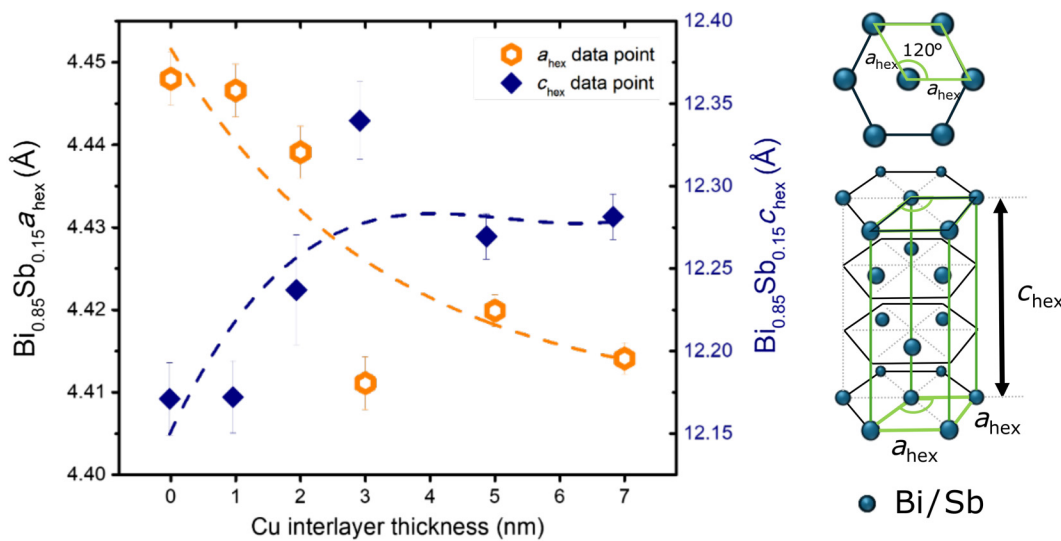


FIG. 8. Lattice parameters  $a_{\text{hex}}$  (orange hexagon) and  $c_{\text{hex}}$  (blue diamond) of the BiSb lattice unit cell (green) as the Cu interlayer below it increases in thickness.

We infer that the largest mismatch between  $\text{Bi}_{0.85}\text{Sb}_{0.15}$  and Cu causes the largest strain in  $\text{Bi}_{0.85}\text{Sb}_{0.15}$  grown atop the Cu interlayer.

In Fig. 6(f), the BiSb-to-interlayer  $a_{\text{hex}}$  ratio is decreased by 0.20% when Cu is the interlayer, followed by  $-0.02\%$  and  $+0.02\%$  for the Ti and Pt interlayer, respectively. Values for the lattice constants of each of the interlayer materials, i.e., Ti (hexagonal phase), Cu (cubic phase), and Pt (cubic fcc phase), were obtained from the Materials Project [56] database. The larger lattice mismatches between BiSb and the Pt and Ti interlayers resulted in an increased peak broadening [Fig. 5(b)] by 1.0%–1.2% and 3.0%–3.7%, respectively.

The  $\text{Bi}_{0.85}\text{Sb}_{0.15}(012)$  peaks for all the Cu interlayer thicknesses were higher than in the no interlayer case [Fig. 7(a)]. Meanwhile, Fig. 7(b) shows that there was

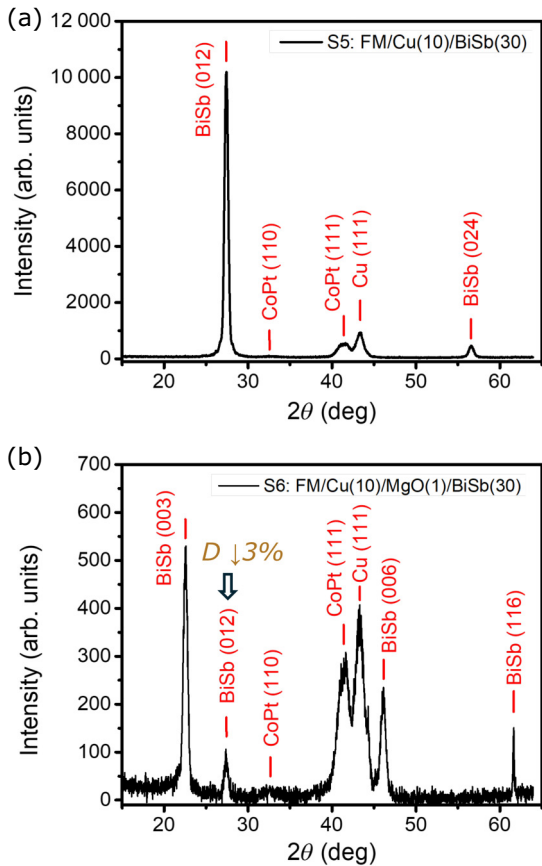


FIG. 9. XRD plots of the intensity against  $2\theta$  for the samples (a) S5 and (b) S6, with a drop displayed in the  $\text{BiSb}(012)$  crystallite size  $D = K\lambda/\beta \cos(\theta)$  by 3.32%. The crystallite size was calculated by the Scherrer equation, where  $K = 0.9$  is the Scherrer constant, and was used throughout all the crystallite size calculations. Here,  $\lambda$  represents the wavelength of emitted x-rays from the Cu anode in the Rigaku XRD system used for measurements, which is 1.54 Å. Moreover,  $\beta$  is the fitted  $2\theta$  FWHM of the  $\text{BiSb}(012)$  peaks in (a) and (b) and  $\theta$  is the Bragg angle; both quantities are expressed in radians.

a plateauing of the full-width half maximum (FWHM), settling around  $0.38^\circ$  from 1 to 5 nm, with the peak broadening beyond 5 nm by increases of  $\sim 1\%$ . The results of this data were used to calculate the lattice constants for  $\text{Bi}_{0.85}\text{Sb}_{0.15}$  in the Cu interlayer samples.

The  $a_{\text{hex}}$  and  $b_{\text{hex}}$  parameters of the hexagonal  $\text{Bi}_{0.85}\text{Sb}_{0.15}$  unit cell lattice change as Cu increases beyond 2 nm (Fig. 8). The intraplanar spacing  $a_{\text{hex}}$  in  $\text{Bi}_{0.85}\text{Sb}_{0.15}$  tends to decrease with increasing Cu thickness below it while  $c_{\text{hex}}$  increases. Thus, the hexagonal  $\text{Bi}_{0.85}\text{Sb}_{0.15}$  unit cell stretches along  $c_{\text{hex}}$  while being compressed along  $a_{\text{hex}}$  whenever Cu increases in thickness by another few Angstroms. In the  $\text{Bi}_{0.85}\text{Sb}_{0.15}$  lattice, a previously increasing  $c_{\text{hex}}$  plateaus around 4.43 Å while  $a_{\text{hex}}$  continues to drop from 5-nm Cu to 7-nm Cu; this means there is now only an intraplanar compression without a stretching along  $c_{\text{hex}}$ . The decrease in  $\text{Bi}_{0.85}\text{Sb}_{0.15}(012)$  crystalline size after 7 nm corresponds to the drop in  $\xi_{\text{DL}}^j$  beyond 7 nm.

The use of the MgO insertion layer in Sample S6 of Fig. 4(a) aims to exclude the potential Cu/ $\text{Bi}_{0.85}\text{Sb}_{0.15}$  interfacial effects. Figure 9 reveals that the insertion of this MgO layer in Sample S6 leads to a measured 3% reduction in the  $\text{Bi}_{0.85}\text{Sb}_{0.15}(012)$  crystallite size, as quantified from the FWHM of the XRD patterns in our measurements from Fig. 9. Despite this minor crystallinity degradation, the spin Hall angle in Fig. 4(a) remains at 37, retaining 75% of the improvement attributed to the  $\text{Bi}_{0.85}\text{Sb}_{0.15}$  layer in the Cu/BiSb sample. This result supports the explanation that interfacial effects from the Cu/BiSb interface are not the primary contributors to the observed spin-torque efficiency.

- [1] S. Murakami, Two-dimensional topological insulators and their edge states, *J. Phys.: Conf. Ser.* **302**, 012019 (2011).
- [2] R. Roy,  $Z_2$  classification of quantum spin Hall systems: An approach using time-reversal invariance, *Phys. Rev. B* **79**, 195321 (2009).
- [3] C. L. Kane and E. J. Mele, Quantum spin Hall effect in graphene, *Phys. Rev. Lett.* **95**, 226801 (2005).
- [4] L. Fu, C. L. Kane, and E. J. Mele, Topological insulators in three dimensions, *Phys. Rev. Lett.* **98**, 106803 (2007).
- [5] R. Roy, Topological phases and the quantum spin Hall effect in three dimensions, *Phys. Rev. B* **79**, 195322 (2009).
- [6] J. E. Moore and L. Balents, Topological invariants of time-reversal-invariant band structures, *Phys. Rev. B* **75**, 121306(R) (2007).
- [7] S. Murakami, Phase transition between the quantum spin Hall and insulator phases in 3D: emergence of a topological gapless phase, *New J. Phys.* **9**, 356 (2007).
- [8] X.-L. Qi and S.-C. Zhang, The quantum spin Hall effect and topological insulators, *Phys. Today* **63** (1), 33 (2010).
- [9] M. Z. Hasan and C. L. Kane, Colloquium: topological insulators, *Rev. Mod. Phys.* **82**, 3045 (2010).
- [10] L. Fu and C. L. Kane, Topological insulators with inversion symmetry, *Phys. Rev. B* **76**, 045302 (2007).

- [11] D. Hsieh, D. Qian, L. Wray, Y. Xia, Y. S. Hor, R. J. Cava, and M. Z. Hasan, A topological Dirac insulator in a quantum spin Hall phase, *Nature* **452**, 970 (2008).
- [12] Y. Xia, D. Qian, D. Hsieh, L. Wray, A. Pal, H. Lin, A. Bansil, D. Grauer, Y. S. Hor, R. J. Cava, and M. Z. Hasan, Observation of a large-gap topological-insulator class with a single Dirac cone on the surface, *Nat. Phys.* **5**, 398 (2009).
- [13] H. Zhang, C.-X. Liu, X.-L. Qi, X. Dai, Z. Fang, and S.-C. Zhang, Topological insulators in  $\text{Bi}_2\text{Se}_3$ ,  $\text{Bi}_2\text{Te}_3$  and  $\text{Sb}_2\text{Te}_3$  with a single Dirac cone on the surface, *Nat. Phys.* **5**, 438 (2009).
- [14] J. Cayssol, Introduction to Dirac materials and topological insulators/Introduction aux matériaux de Dirac et aux isolants topologiques, *C. R. Phys.* **14**, 760 (2013).
- [15] X.-L. Qi and S.-C. Zhang, Topological insulators and superconductors, *Rev. Mod. Phys.* **83**, 1057 (2011).
- [16] M. Ezawa, Y. Tanaka, and N. Nagaosa, Topological phase transition without gap closing, *Sci. Rep.* **3**, 2790 (2013).
- [17] B. A. Bernevig and T. L. Hughes, *Topological Insulators and Topological Superconductors* (Princeton University Press, Princeton, 2013).
- [18] D. Ovchinnikov, J. Cai, Z. Lin, Z. Fei, Z. Liu, Y.-T. Cui, D. H. Cobden, J.-H. Chu, C.-Z. Chang, D. Xiao, J. Yan, and X. Xu, Topological current divider in a Chern insulator junction, *Nat. Commun.* **13**, 5967 (2022).
- [19] Y. Wang, Broken-symmetry states in topological insulators, *Mod. Phys. Lett. B* **29** (25), 1530006 (2015).
- [20] A. L. Araújo, F. Crasto de Lima, C. H. Lewenkopf, and A. Fazzio, Design of spin-orbital-textures in ferromagnetic/topological insulator interfaces, *Phys. Rev. B* **109**, 085142 (2024).
- [21] P. S. Mandal, G. Springholz, V. V. Volobuev, O. Caha, A. Varykhalov, E. Golias, G. Bauer, O. Rader, and J. Sánchez-Barriga, Topological quantum phase transition from mirror to time reversal symmetry protected topological insulator, *Nat. Commun.* **8**, 968 (2017).
- [22] S. Zhang and Z. Yang, Intrinsic spin and orbital angular momentum Hall effect, *Phys. Rev. Lett.* **94**, 066602 (2005).
- [23] B. A. Bernevig, T. L. Hughes, and S.-C. Zhang, Orbitronics: The intrinsic orbital current in p-doped silicon, *Phys. Rev. Lett.* **95**, 066601 (2005).
- [24] H. Kontani, T. Tanaka, D. Hirashima, K. Yamada, and J. Inoue, Giant orbital Hall effect in transition metals: origin of large spin and anomalous Hall effects, *Phys. Rev. Lett.* **102**, 016601 (2009).
- [25] D. Go, D. Jo, C. Kim, and H.-W. Lee, Intrinsic spin and orbital Hall effects from orbital texture, *Phys. Rev. Lett.* **121**, 086602 (2018).
- [26] A. Razavi, H. Wu, Q. Shao, C. Fang, B. Dai, K. Wong, X. Han, G. Yu, and K. L. Wang, Deterministic spin-orbit torque switching by a light-metal insertion, *Nano Lett.* **20**, 3703 (2020).
- [27] S. Krishnia, Y. Sassi, F. Ajedas, N. Sebe, N. Reyren, S. Collin, T. Denneulin, A. Kovács, R. E. Dunin-Borkowski, A. Fert, J.-M. George, V. Cros, and H. Jaffrè, Large interfacial Rashba interaction generating strong spin-orbit torques in atomically thin metallic heterostructures, *Nano Lett.* **23**, 6785 (2023).
- [28] Y. Xu, F. Zhang, A. Fert, H.-Y. Jaffrè, Y. Liu, R. Xu, Y. Jiang, H. Cheng, and W. Zhao, Orbitronics: light-induced orbital currents in Ni studied by terahertz emission experiments, *Nat. Commun.* **15**, 2043 (2024).
- [29] R. Chen, D. Go, S. Blügel, W. Zhao, and Y. Mokrousov, Dzyaloshinskii-Moriya interaction from unquenched orbital angular momentum, *Phys. Rev. B* **109**, 144417 (2024).
- [30] S. Krishnia, B. Bony, E. Rongione, L. M. Vicente-Arche, T. Denneulin, A. Pezo, Y. Lu, R. E. Dunin-Borkowski, S. Collin, A. Fert, J.-M. George, N. Reyren, V. Cros, and H. Jaffrè, Quantifying the large contribution from orbital Rashba-Edelstein effect to the effective damping-like torque on magnetization, *APL Mater.* **12**, 051105 (2024).
- [31] D. Lee, D. Go, H.-J. Park, W. Jeong, H.-W. Ko, D. Yun, D. Jo, S. Lee, G. Go, J. H. Oh, K.-J. Kim, B.-G. Park, B.-C. Min, H. C. Koo, H.-W. Lee, O. Lee, and K.-J. Lee, Orbital torque in magnetic bilayers, *Nat. Commun.* **12**, 6710 (2021).
- [32] H. Hayashi, D. Jo, D. Go, T. Gao, S. Haku, Y. Mokrousov, H.-W. Lee, and K. Ando, Observation of long-range orbital transport and giant orbital torque, *Commun. Phys.* **6**, 32 (2023).
- [33] A. Bose, F. Kammerbauer, R. Gupta, D. Go, Y. Mokrousov, G. Jakob, and M. Kläui, Detection of long-range orbital-Hall torques, *Phys. Rev. B* **107**, 134432 (2023).
- [34] Y.-G. Choi, D. Jo, K.-H. Ko, D. Go, K.-H. Kim, H. G. Park, C. Kim, B.-C. Min, G.-M. Choi, and H.-W. Lee, Observation of the orbital Hall effect in a light metal Ti, *Nature* **619**, 52 (2023).
- [35] H. Hayashi and K. Ando, Orbital Hall magnetoresistance in Ni/Ti bilayers, *Appl. Phys. Lett.* **123**, 172401 (2023).
- [36] D. Jo, D. Go, and H.-W. Lee, Gigantic intrinsic orbital Hall effects in weakly spin-orbit coupled metals, *Phys. Rev. B* **98**, 214405 (2018).
- [37] F. Tuo, H. D. K. Nguyen, N. Soichiro, and N. H. Pham, Ultrahigh efficient spin orbit torque magnetization switching in fully sputtered topological insulator and ferromagnet layers, *Sci. Rep.* **12**, 2998 (2020).
- [38] H. Wu, P. Zhang, P. Deng, Q. Lan, Q. Pan, S. A. Razavi, X. Che, L. Huang, B. Dai, K. Wong, X. Han, and K. L. Wang, Room-temperature spin-orbit torque from topological surface states, *Phys. Rev. Lett.* **123**, 207205 (2019).
- [39] P. Li, J. Kally, S. S.-L. Zhang, T. Pillsbury, J. Ding, G. Csaba, J. Ding, J. S. Jiang, Y. Liu, and M. Wu, Magnetization switching using topological surface states, *Sci. Adv.* **5**, eaaw3415 (2019).
- [40] N. H. D. Khang, Y. Ueda, and N. H. Pham, A conductive topological insulator with large spin Hall effect for ultralow power spin-orbit torque switching, *Nat. Mater.* **17**, 808 (2018).
- [41] H. Wu, A. Chen, P. Zhang, H. He, J. Nance, C. Guo, J. Sasaki, T. Shirokura, N. H. Pham, B. Fang, S. A. Razavi, K. Wong, Y. Wen, Y. Ma, G. Yu, G. P. Carman, X. Han, X. Zhang, and K. L. Wang, Magnetic memory driven by topological insulators, *Nat. Commun.* **12**, 6251 (2021).
- [42] H. H. Huy, R. Zhang, S. Takanori, T. Shigeki, H. Yoshiyuki, and N. H. Pham, Integration of BiSb topological insulator and CoFeB/MgO with perpendicular anisotropy using an oxide interfacial layer for ultralow power SOT-MRAM cache memory, *IEEE Trans. Magn.* **59**, 3400905 (2023).
- [43] H. H. Huy, J. Sasaki, N. H. D. Khang, S. Namba, P. N. Hai, Q. Le, B. York, C. Hwang, X. Liu, M. Gribelyuk, X. Xu,

- S. Le, N. Nagabhivara, M. Ho, and H. Takano, Large spin Hall angle in sputtered BiSb topological insulator on top of various ferromagnets with in-plane magnetization for sot reader application, *IEEE Trans. Magn.* **59**, 3000904 (2023).
- [44] F. Binda, S. Fedel, S. F. Alvarado, P. Noël, and P. Gambardella, Spin-orbit torques and spin Hall magnetoresistance generated by twin-free and amorphous  $\text{Bi}_{0.9}\text{Sb}_{0.1}$  topological insulator films, *Adv. Mater.* **35**, 2304905 (2023).
- [45] N. H. D. Khang, S. Nakano, T. Shirokura, Y. Miyamoto, and P. N. Hai, Ultralow power spin-orbit torque magnetization switching induced by a non-epitaxial topological insulator on Si substrates, *Sci. Rep.* **10**, 12185 (2020).
- [46] S. Goel, N. H. D. Khang, Y. Osada, L. D. Anh, P. N. Hai, and M. Tanaka, Room-temperature spin injection from a ferromagnetic semiconductor, *Sci. Rep.* **13**, 2181 (2023).
- [47] R. Zhang, H. H. Huy, T. Shirokura, P. N. Hai, Q. Le, B. York, C. Hwang, X. Liu, M. Gribelyuk, X. Xu, S. Le, M. Maeda, T. Fan, Y. Tao, and H. Takano, High spin Hall angle in BiSb topological insulator and perpendicularly magnetized CoFeB/MgO multilayers with metallic interfacial layers, *Appl. Phys. Lett.* **124**, 072402 (2024).
- [48] Z. Chi, Y.-C. Lau, X. Xu, T. Ohkubo, K. Hono, and M. Hayashi, The spin Hall effect of BiSb alloys driven by thermally excited Dirac-like electrons, *Sci. Adv.* **6**, aay2324 (2020).
- [49] P. N. Hai, Spin Hall effect in topological insulators, *J. Mag. Soc. Jpn* **44**, 137 (2020).
- [50] H. Y. Poh, C. C. I. Ang, G. J. Lim, T. L. Jin, S. H. Lee, E. K. Koh, F. Poh, and W. S. Lew, Crystallinity control of the topological-insulator surface  $\text{Bi}_{85}\text{Sb}_{15}(012)$  via interfacial engineering for enhanced spin-orbit torque, *Phys. Rev. Appl.* **19**, 034012 (2023).
- [51] M. Hayashi, J. Kim, M. Yamanouchi, and H. Ohno, Quantitative characterization of the spin-orbit torque using harmonic Hall voltage measurements, *Phys. Rev. B* **89**, 144425 (2014).
- [52] U. Holzwarth and N. Gibson, The Scherrer equation versus the ‘Debye-Scherrer equation’, *Nat. Nanotechnol.* **6**, 534 (2011).
- [53] R. Q. Zhang, *et al.*, Current-induced magnetization switching in a CoTb amorphous single layer, *Phys. Rev. B* **101**, 214418 (2020).
- [54] T.-Y. Chen, Y. Ou, T.-Y. Tsai, R. A. Buhrman, and C.-F. Pai, Spin-orbit torques acting upon a perpendicularly magnetized Py layer, *APL Mater.* **6**, 121101 (2018).
- [55] T. Jin, G. J. Lim, H. Y. Poh, F. Tan, and W. S. Lew, Spin reflection-induced field-free magnetization switching in perpendicularly magnetized MgO/Pt/Co heterostructures, *ACS Appl. Mater. Interfaces* **14**, 9781 (2022).
- [56] A. Jain, S. P. Ong, G. Hautier, W. Chen, W. D. Richards, S. Dacek, S. Cholia, D. Gunter, D. Skinner, G. Ceder, and K. A. Persson, Commentary: The materials project: A materials genome approach to accelerating materials innovation, *APL Mater.* **1**, 011002 (2013).